Interior–Exterior Asymmetry and Planar Equivalence in Rough-Wall Plasma Sheaths

Pei Qiu[1] and Chang Lu[2,*]

[1] College of Zhan Tianyou, Dalian Jiaotong University, Dalian, 116028, China
[2] State Key Laboratory of Industrial Equipment Structural Analysis and Optimization and CAE Software, Dalian University of Technology, Dalian, 116024, China

Classical one-dimensional (1D) planar sheath laws underpin macroscopic plasma modeling, yet they are widely believed to break down when roughness reaches the intermediate-scale regime where near-wall fields and ion trajectories become strongly multidimensional. Furthermore, no rigorous criterion exists to define this intermediate-scale roughness regime. Here we reveal an asymmetry between the sheath interior and exterior: for cold-ion Debye sheaths over the rough walls considered here, we prove that even with a strongly multidimensional sheath interior, a single planar sheath can always reproduce the exterior plasma response, provided the maximum relative variation of the normal electric field across the inlet is below the prescribed tolerance. Consequently, at fixed inlet conditions and tolerance, the inlet-field variation provides a rigorous criterion defining the intermediate-scale roughness regime. For intermediate-scale roughness where planar equivalence fails, we further derive a pointwise transport correction to the classical 1D sheath equation. Numerical simulations verify the effective plane and validate the correction for near-wall ion density and wall flux. By unifying exterior planar equivalence, its breakdown criterion, and the pointwise transport correction, this theory links microscopic ion dynamics near rough walls to the macroscopic plasma response.

I. INTRODUCTION

A thin sheath regulates particle and energy fluxes to a material wall[1–3] and supplies boundary conditions for models of the quasineutral plasma[4–6]. Classical planar sheath theory assumes variation only along the wall normal, as in the space-charge laws[7, 8]. Real walls, however, deviate from this ideal plane as etching, deposition, and erosion produce surface roughness[9–11]. This planar picture still holds for small-amplitude ripples or gently curved surfaces under local tangent-plane approximation [12]. By contrast, once surface roughness approaches the sheath scale, substantial near-wall field distortions and ion deflections are commonly taken to invalidate planar sheath models[13–17].

Yet such near-wall distortions need not preclude planar behavior farther out [18]. Figure 1 (a)-(b) demonstrates this paradox: even when peak-to-valley height and spacings are comparable to the sheath thickness, the pointwise exterior response to the rough wall is well captured by a single effective plane. This reveals a striking inner–outer asymmetry: strong near-wall multidimensionality can coexist with a planar exterior. The natural questions are when such planar equivalence holds or fails, and what rigorously defines the corresponding boundary. While rough-boundary electrostatics admits effective planes [19, 20], a plasma sheath nonlinearly couples the field to directed ion flow; prior multidimensional sheath studies—spanning curved walls [21, 22], emission or radio-frequency forcing [23–25], and numerical resolution [26]—have focused on regime-specific structure rather than a criterion for planar equivalence.

Here, for cold-ion Debye sheaths, we establish a rigorous criterion that defines the intermediate-scale roughness regime. When planar equivalence holds, we provide the procedure to locate the effective plane. Otherwise, we further derive a pointwise transport correction to capture the near-wall ion density and local wall flux.

II. ROUGH-WALL SHEATH MODEL AND INLET CONDITIONS

In Figure 1, z increases toward the flat inlet at $z = H$. The rough wall Γ_w projects onto $\Omega_\perp \subset \mathbb{R}^m$ in the inlet plane. Its height $h(\boldsymbol{x}_\perp)$ depends on one transverse coordinate in two dimensions ($m = 1$) or two in three dimensions ($m = 2$). We assume

$$\Gamma_w : z = h(\boldsymbol{x}_\perp), \quad h \in W^{1,\infty}(\Omega_\perp), \quad H - \sup h \geq d_0 > 0. \tag{1}$$

Bounded height and slope allow steep faces and corners. The inlet lies at least d_0 above the highest peak. We compare solutions pointwise above a fixed finite patch $D \subseteq \Omega_\perp$. Sheath-scale heights and peak spacings are comparable to L_{sh}, the planar sheath thickness at the same bias and supply. We measure L_{sh} from the reference wall at $z = 0$ to the edge where the fractional charge imbalance $1 - n_{e,c}/n_{i,c}$ reaches $\chi = 0.05$. Here $n_{e,c}$ and $n_{i,c}$ are the classical planar electron and ion densities. The subscript c denotes the planar solution.

On the bounded observation region we use the Lipschitz representative of the wall height. The wall potential is imposed as a boundary trace. The field and trajectory equations are used in the plasma, with the regularity required below imposed on the solution in the region where each estimate is applied.

* Corresponding author: changlu@dlut.edu.cn

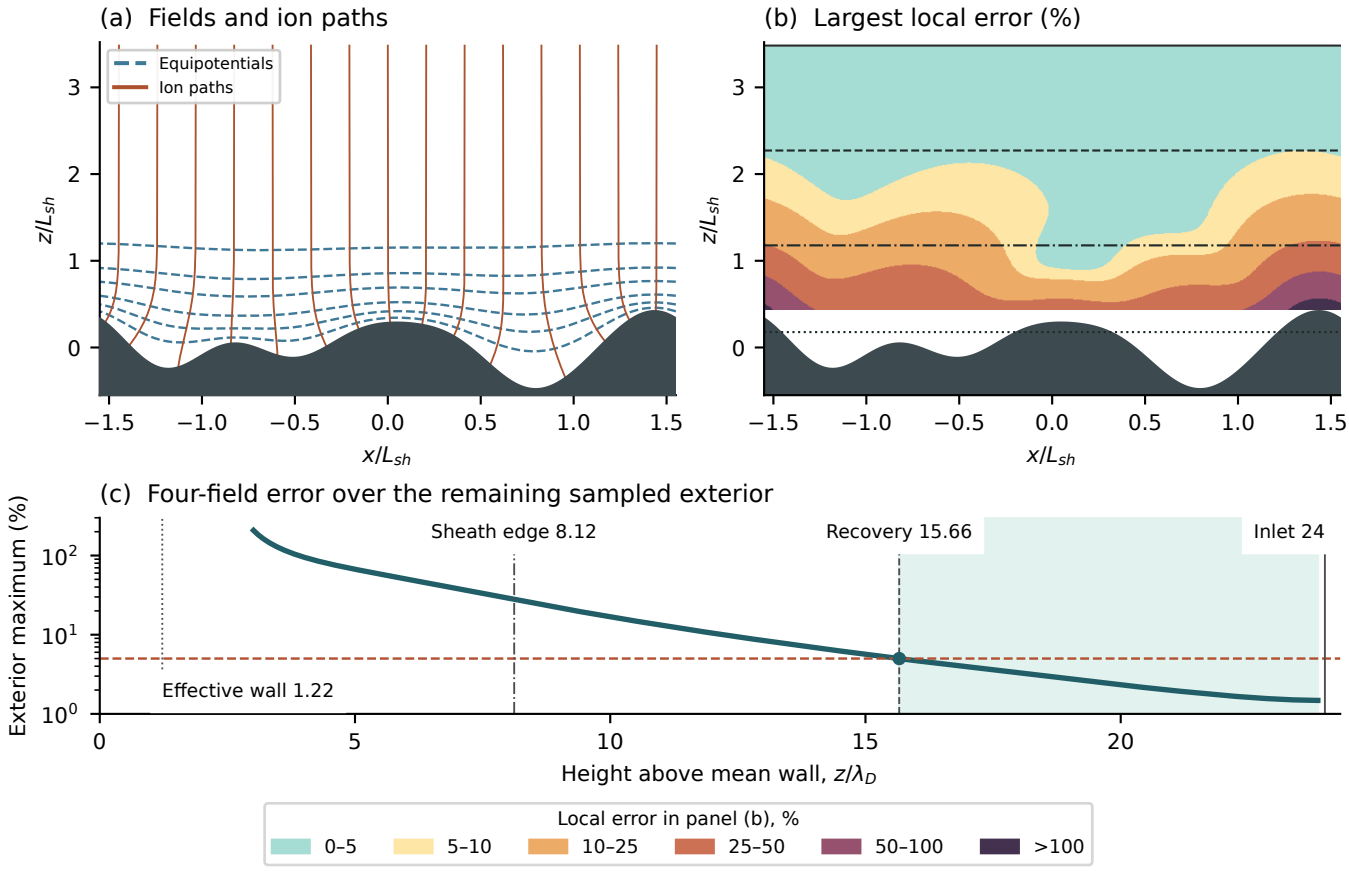


Figure 1. Pointwise exterior equivalence above a three-peak wall. Panels (a) and (b) show the same wall profile with a common aspect ratio. (a) Equipotentials and ion trajectories from the independent reference solution. (b) At each plasma sample, the color gives the largest of the four normalized errors relative to one predicted plane. Gray is the wall; white is outside the sampled sections. Horizontal lines mark the effective wall (dotted), reconstructed sheath edge (dash-dotted), first passing section (dashed) and inlet (solid). (c) Maximum over the patch, the four quantities and all remaining sampled heights. Shading extends from the first passing section to the last tested section.

The sheath is steady, electrostatic, collisionless, and unmagnetized. The absorbing wall is held at $V < 0$ and emits no electrons. At the inlet the potential is $\phi = 0$ and the electron supply is Maxwellian. Cold ions of uniform density n_0 enter normally at speed u_{in}, with Mach number $M = u_{\text{in}}/c_s \geq 1$ and ion sound speed c_s. Although the inlet is equipotential, its normal field $E_z = -\partial_z\phi$ can vary across the patch. The rough-wall solution determines this variation.

We measure length in reservoir Debye lengths λ_D, density in units of the incoming Maxwellian density scale, potential in T_e/e, and velocity in the ion sound speed $c_s = \sqrt{T_e/m_i}$ (T_e is the electron temperature in energy units, e the elementary charge, and m_i the ion mass). For regular single-stream flow from the inlet toward the wall, the ion density n_i, velocity $\boldsymbol{u}$, and potential ϕ obey

$$\nabla\cdot(n_i\boldsymbol{u}) = 0, \quad (\boldsymbol{u}\cdot\nabla)\boldsymbol{u} = -\nabla\phi, \quad \nabla^2\phi = F_e(\phi) - n_i. \tag{2}$$

Here $n_e = F_e(\phi)$ is the prescribed local electron density, including the loss of electrons to an absorbing planar wall [27]. Energy conservation fixes the ion speed $W = |\boldsymbol{u}|$ along each trajectory. In the classical planar sheath, conservation of ion flux then gives the reference ion density $f(\phi)$ [28]. These relations give

$$W = \sqrt{M^2 - 2\phi}, \qquad f(\phi) = \frac{n_0 M}{W}, \qquad F_e(\phi) = \frac{e^\phi}{2}\left[1 + \operatorname{erf}\sqrt{\phi - V}\right]. \tag{3}$$

Here erf is the error function. At the inlet both species have density $n_i = n_e = n_0 = F_e(0)$. With bias, supply, and electron response fixed, we test how far toward the wall one planar solution describes the exterior across D.

Here $\boldsymbol{r} = (\boldsymbol{x}_\perp, z)$, $\nabla = (\nabla_\perp, \partial_z)$, and $\boldsymbol{u} = -M\hat{\boldsymbol{z}}$ at the inlet.

III. EXTERIOR PLANAR EQUIVALENCE

A. Selection of the effective plane

An overbar denotes the transverse average over the fixed observation patch $D \subseteq \Omega_\perp$,

$$\bar{a}(z) = \frac{1}{|D|}\int_D a(\boldsymbol{x}_\perp, z)\, d^m x_\perp. \tag{4}$$

Fix the patch D, the finite inlet H, the wall bias $V < 0$, and $M \geq 1$. At the inlet let $a_H(\boldsymbol{x}_\perp) = \partial_z\phi(\boldsymbol{x}_\perp, H)$ and assume $\bar{a}_H > 0$.

Starting at the inlet, we follow the classical planar solution toward the wall. The position where its potential first reaches the prescribed wall potential V defines the effective wall position s_{eff}. The rough-wall transport calculation supplies the mean inlet potential slope $\bar{a}_H$ from the wall geometry, plasma supply, and lateral exchange. With $\phi_c(H) = 0$ and $\phi_c'(H) = \bar{a}_H$, the first integral of the planar Poisson equation gives the distance from the inlet to that wall. Writing $F = F_e - f$ and $U(\phi) = \int_0^\phi F(\psi)\, d\psi$, we obtain on the monotone branch

$$s_{\text{eff}} = H - \int_V^0 \frac{d\psi}{\sqrt{\bar{a}_H^2 + 2U(\psi)}}. \tag{5}$$

Proposition 1 (effective wall selected by the inlet slope). For each inlet slope $a > 0$ there is a unique monotone classical sheath between $p = V$ and $p = 0$. Its virtual wall position is

$$s(a) = H - \ell(a), \qquad \ell(a) = \int_V^0 [a^2 + 2U(p)]^{-1/2} dp. \tag{6}$$

Here $\ell(a) = H - s(a)$ is the distance from the candidate wall to the inlet. The map $a \mapsto s$ is strictly increasing and maps $(0, \infty)$ onto $(-\infty, H)$.

Proof. Put $p = -t < 0$. Since the absorbing-electron factor is nondecreasing in p,

$$F_e(-t) \leq n_0 \exp(-t) < n_0(1+2t/M^2)^{-1/2} = f(-t). \tag{7}$$

The strict inequality follows from $\log(1+2t/M^2) < 2t$ for $t > 0$, $M \geq 1$. Thus $F(p) < 0$, $U(p) > 0$ for $V \leq p < 0$. The positive first-integral branch gives Eq. (6); it is finite for $a > 0$, and

$$s'(a) = a\int_V^0 [a^2 + 2U(p)]^{-3/2} dp > 0. \tag{8}$$

Moreover $U(p) = \kappa^2 p^2/2 + O(p^3)$ near zero, where $\kappa^2 = F_e'(0) - n_0/M^2 > 0$. Consequently $\ell(a) \to \infty$ as $a \downarrow 0$ and $\ell(a) \to 0$ as $a \to \infty$. □

The predicted rough-wall inlet slope therefore fixes $s_{\text{eff}} = s(\bar{a}_H)$. Note that, for a candidate planar wall at s, $d_{\text{cl}}(s)$ is its wall-to-edge distance. The selected wall has $z_{\text{edge}} = s_{\text{eff}} + d_{\text{cl}}(s_{\text{eff}})$, computed in the same classical boundary-value problem using $1 - n_{e,c}/n_{i,c} = \chi = 0.05$. Here λ_D is the normalization length, L_{sh} the nominal-plane reference thickness, and $d_{\text{cl}}(s)$ the reconstructed classical thickness.

B. Pointwise error and inlet criterion

As reference, we select the classical planar solution whose inlet potential and patch-averaged normal field match those of the rough-wall solution over D. At each height z we compare the potential, the full electric-field vector, and the electron and ion density deficits point by point with that solution.

Above the highest peak, the same transverse patch is filled with plasma at every height. We compare the rough-wall solution there with a single classical solution. At heights where all four signal scales are positive, divide each local difference by its corresponding mean rough-wall signal, $D_\phi = |\bar{\phi}|$, $D_E = |\bar{E}_z|$, $D_e = |n_0 - \bar{n}_e|$, and $D_i = |n_0 - \bar{n}_i|$. Since both solutions share n_0, subtracting their density deficits gives the same absolute difference as subtracting their densities. With $\boldsymbol{E}_c = E_{z,c}\hat{\boldsymbol{z}}$, the field difference is the Euclidean norm of $\boldsymbol{E} - E_{z,c}\hat{\boldsymbol{z}}$. The greatest of these four normalized errors over all positions in D is $e_{\max}(z)$. At H the potential and both density deficits vanish, so we use the limit from the plasma side.

With this error measure defined, we next explain why the inlet field governs all four errors. A short distance $y = H - z$ toward the wall, the potential drop from the inlet is $a_H y$ to first order, where the inlet potential slope is $a_H(\boldsymbol{x}_\perp) = \partial_z\phi(\boldsymbol{x}_\perp, H) = -E_z(\boldsymbol{x}_\perp, H)$. The local electron response and cold-ion equations make each density deficit proportional to this drop to first order. The planar solution has the same coefficients, with a_H replaced by its patch mean $\bar{a}_H > 0$. The tangential field tends to zero at the equipotential inlet, so the relative error in the full field vector has the same limit.

Theorem 2 (pointwise recovery on a finite patch). Suppose $H > z_{\text{edge}}$ and the regular inlet solution has uniform Taylor remainders on the closure of D in one or two transverse dimensions. Use the plane selected by $\bar{a}_H$. For $u_j = \phi, \boldsymbol{E}, n_e, n_i$, the limiting error is

$$\begin{aligned} e_{\max}(z) &= \max_j \frac{\sup_{\boldsymbol{x}_\perp \in D} |u_j(\boldsymbol{x}_\perp, z) - u_{j,c}(z)|}{D_j(z)}, \\ \lim_{z\uparrow H} e_{\max}(z) &= \delta_D(H) = \frac{\sup_{\boldsymbol{x}_\perp \in D} |a_H(\boldsymbol{x}_\perp) - \bar{a}_H|}{\bar{a}_H}. \end{aligned} \tag{9}$$

Here $|\cdot|$ denotes the Euclidean norm for $\boldsymbol{E}$. For a prescribed relative tolerance $\epsilon > 0$, if $\delta_D(H) < \epsilon$, some z_m with $z_{\text{edge}} < z_m < H$ satisfies $e_{\max}(z) \leq \epsilon$ for all $z_m \leq z < H$.

Proof. Move a distance $y = H - z$ from the uniform inlet toward the wall. The local slope a_H sets the leading potential drop, and the electron response and cold-ion balances give the leading density deficits,

$$\begin{aligned} \phi &= -a_H(\boldsymbol{x}_\perp)y + O(y^2), \\ n_i &= n_0 - \frac{n_0 a_H(\boldsymbol{x}_\perp)}{M^2}y + O(y^2), \\ n_e &= n_0 - F_e'(0)a_H(\boldsymbol{x}_\perp)y + O(y^2). \end{aligned} \tag{10}$$

The classical solution has the same three expansions with a_H replaced by $\bar{a}_H$. Thus each absolute scalar discrepancy is $K_j|a_H - \bar{a}_H|y + O(y^2)$, while its normalization is $K_j\bar{a}_H y + O(y^2)$, with $K_\phi = 1$, $K_e = F_e'(0)$, and $K_i = n_0/M^2$. Dividing cancels the common factor $K_j y$. The local relative error tends to $|a_H - \bar{a}_H|/\bar{a}_H$ even though the signals themselves vanish.

For the field, $\nabla_\perp \phi = 0$ at the equipotential inlet. The potential and normal field relative to their patch means satisfy

$$\begin{aligned} \phi - \bar{\phi} &= -(a_H - \bar{a}_H)y + O(y^2), \\ E_z - \bar{E}_z &= -(a_H - \bar{a}_H) + O(y). \end{aligned} \tag{11}$$

The classical normal field tends to $-\bar{a}_H$, the transverse field is $O(y)$, and $D_E = \bar{a}_H + O(y)$. The vector error therefore has the same normalized limit as the three scalar errors. The remainders are uniform on D, so taking the supremum across the patch and then the maximum over the four quantities gives Eq. (9). If $\delta_D(H) < \epsilon$, the positive margin $\epsilon - \delta_D(H)$ supplies a nonempty interval above the edge on which all four errors stay within tolerance. The width and the remaining mean deficits depend on the solution. If $\delta_D(H) > \epsilon$, the limit $e_{\max}(z) \to \delta_D(H)$ as $z \uparrow H$ implies that every interval extending to the inlet contains cross sections where $e_{\max}(z) > \epsilon$. □

Thus, as $z \uparrow H$, $e_{\max}(z)$ tends to the maximum relative deviation of the inlet normal field from its patch mean, as illustrated in Figure 1(c). Fix the patch, inlet, bias, supply, and tolerance $\epsilon > 0$, with the inlet above the reconstructed sheath edge. If $\delta_D(H) > \epsilon$, the selected plane fails to meet tolerance on any interval extending to the inlet. This defines the intermediate-scale roughness regime for exterior planar replacement. We assign $\delta_D(H) \le \epsilon$ to the complementary class. $\delta_D(H) < \epsilon$ guarantees an interval above the sheath edge on which all four quantities meet tolerance everywhere across D and at every height up to the inlet ($z < H$). At $\delta_D(H) = \epsilon$ the error profile determines whether such an interval exists.

C. Recovery height

Keeping this plane fixed, we compare its solution with the rough-wall fields at each height in their common plasma domain above the peaks. Starting just below the inlet and moving toward the wall, we require all four fields to stay within tolerance everywhere across D. The recovery height z_{rec} is the lower limit of this interval,

$$z_{\mathrm{rec}} = \inf\{z : \sup_{z \le t < H} e_{\max}(t) \le \epsilon\}. \tag{12}$$

Note that the charge-imbalance threshold χ locates the reconstructed planar sheath edge z_{edge}, and an exterior plasma calculation places its interface at a height z_m satisfying $\max\{z_{\mathrm{edge}}, z_{\mathrm{rec}}\} < z_m < H$.

IV. POINTWISE TRANSPORT CORRECTION WHERE PLANAR EQUIVALENCE FAILS

At a given potential, energy conservation fixes the ion speed W. The local ion density also depends on how closely neighboring trajectories converge and how fast the ions cross a horizontal section. Follow a narrow tube of trajectories from the inlet to height z. Let J be the ratio of its horizontal cross-sectional area to its inlet area (a width ratio in two dimensions). Let $\mu = |u_z|/W$ denote the cosine of the angle between the ion velocity and the downward normal to the inlet plane, where u_z is the z component of the ion velocity.

For an inlet area dA_H, the tube occupies an area $J\,dA_H$, and the ions cross it with downward speed $|u_z| = W\mu$, where energy conservation fixes $W = |\boldsymbol{u}| = \sqrt{M^2 - 2\phi}$.

The ion rate through the tube is conserved. With the planar density $f(\phi) = n_0 M/W$, this gives

$$n_i|u_z|J = n_0 M, \qquad n_i = f(\phi)G, \qquad G = (J\mu)^{-1}. \tag{13}$$

At fixed potential, contraction of the tube raises the density. At fixed tube area and speed, a more oblique crossing also raises the density because μ decreases. This relation applies where inlet-connected trajectories cross downward and the map from the inlet to the section is one-to-one with $J > 0$.

To compute J, label each trajectory by its inlet position $\boldsymbol{a}$ and write $\boldsymbol{X}_\perp(\boldsymbol{a}, z)$ for its transverse position at height z. Its transverse displacement per unit change in height is $\boldsymbol{v} = \boldsymbol{u}_\perp/u_z$. The matrix $\mathsf{A} = \partial \boldsymbol{X}_\perp/\partial \boldsymbol{a}$ tracks the separation of neighboring trajectories, and its determinant gives the area ratio.

$$\partial_z \boldsymbol{X}_\perp = \boldsymbol{v}(\boldsymbol{X}_\perp, z), \qquad \boldsymbol{X}_\perp(\boldsymbol{a}, H) = \boldsymbol{a}, \tag{14}$$

$$\partial_z \mathsf{A} = (D_\perp \boldsymbol{v})\mathsf{A}, \qquad J = \det \mathsf{A}, \qquad \partial_z \ln J = \nabla_\perp \cdot \boldsymbol{v}. \tag{15}$$

The direction of motion $\boldsymbol{t} = \boldsymbol{u}/W$ gives $\mu = |t_z|$. Projecting the ion momentum equation perpendicular to $\boldsymbol{t}$ shows how the electric field turns the trajectory.

$$(\boldsymbol{t} \cdot \nabla)\boldsymbol{t} = -\frac{(\mathsf{I} - \boldsymbol{t} \otimes \boldsymbol{t})\nabla\phi}{W^2}. \tag{16}$$

Substituting this density into Poisson's equation gives the potential curvature along the reference normal z,

$$\phi_{zz} = F_e(\phi) - f(\phi) - \nabla_\perp^2 \phi + f(\phi)(1 - G). \tag{17}$$

The first two terms give the classical planar charge response. The Laplacian $\nabla_\perp^2$ in the transverse coordinates accounts for lateral variation of the potential, and $f(\phi)(1 - G)$ accounts for the change in ion density due to convergence or deflection along the trajectories. For planar flow, ions travel along parallel paths normal to the wall, $G = J = \mu = 1$, and the last two terms vanish.

The two-dimensional predictor estimates the ion direction from the wall geometry and inlet supply to evaluate the correction (Sec. V A).

Follow the same tube to the wall. Its ion collection rate is $n_0 M\, dA_H$. If its landing area has horizontal projection $dA_{w,\perp}$, the local flux per unit projected wall area, normalized by $n_0 M$ as in Figure 5(f), is $dA_H/dA_{w,\perp}$. The density calculation uses the tube area $J\, dA_H$ at a single height. The wall-flux calculation uses the landing positions, whose heights vary along the rough wall.

V. NUMERICAL METHODS AND VERIFICATION

A. Wall profiles and numerical methods

For the three-peak wall, we test how far toward the wall the planar solution selected at the inlet reproduces all four fields across the patch.

Three-peak wall and inlet conditions. The three-peak wall has a peak-to-valley height of $0.90L_{sh}$ and successive peak spacings of 1.389, 0.844, and $0.867L_{sh}$. The numerical tests use one transverse coordinate. For Figures 1–3, $M = 1.2$, $V = -5$, $L_{sh} = 6.8938\lambda_D$, and the inlet is $24\lambda_D$ above the mean wall. We set $L = 3.10L_{sh}$ and scale L_{amp} to the specified peak-to-valley height in $h(x) = L_{\mathrm{amp}} \sum_{j=1}^{5} b_j \cos(2\pi jx/L + \beta_j)$. The coefficients and phases (in radians) are

$$(b_1, \ldots, b_5) = (0.055, 0.26, 0.18, 0.07, 0.035),$$
$$(\beta_1, \ldots, \beta_5) = (1.10, 0.15, -1.70, 0.95, 2.45)$$

The four comparison walls share a spectral shape and differ only in amplitude. They use $h(x) = B\sum_j b_j \cos(2\pi jx/L + \beta_j)$ on the full patch of length $L = 14.377025L_{sh}$. In the first four rows of Table I, $B/L_{sh} = 0.0625, 0.125, 0.5, 1$, respectively; the measured amplitudes A/L_{sh} appear in Table III. All four walls use the relative amplitudes b_j and phases β_j listed below, with phases in radians. Only the overall height factor B varies. The six successive peak spacings include the distance from the last peak to the first across the patch boundary. Their mean is $L/6 = 2.39617L_{sh}$.

j	b_j	β_j	j	b_j	β_j
1	0.34054147	−1.99642424	9	0.06400792	−0.88374132
2	0.31338936	−1.86185777	10	0.03846572	0.81058897
3	0.27808868	−1.44361041	11	0.02008642	2.61784228
4	0.24060286	2.12099409	12	0.00883242	−1.01927427
5	0.20319898	−2.65272432	13	0.00316021	−2.72395997
6	0.16624135	−2.55956398	14	0.00088649	−0.48868770
7	0.12992810	2.43483879	15	0.00018732	−0.66212151
8	0.09522594	2.59741991	16	0.00002856	−0.77335860

Predictor and reference solution. From the wall profile and inlet conditions, the predictor computes the mean inlet slope that selects the effective plane. Independently, we solve the coupled trajectory–Poisson problem on two grids, starting from the planar solution and increasing the roughness from quarter to full amplitude. We compare all four reference fields on both grids with the same inlet-selected planar solution.

The predictor estimates the direction of ion motion from the velocity potential. At speed $W = \sqrt{M^2 - 2\phi}$, its initial approximation uses

$$\Psi_0 = \int_z^H W\, dz', \qquad \Psi_2 = -\frac{1}{2}\int_z^H \frac{|\nabla_\perp \Psi_0|^2}{W}\, dz'. \quad (18)$$

The transverse velocity is obtained from $\nabla_\perp(\Psi_0 + \Psi_2)$, and the downward component is selected by energy conservation. In mapped coordinates $z = h(x) + \alpha(x)\xi$, set $\alpha = 1 - h/H$, $b = (1 - \xi/H)h'$, and $\boldsymbol{u} = -W(\sin\theta, \cos\theta)$. Here ∂_x holds ξ fixed. Projecting Eq. (16) onto $(-\cos\theta, \sin\theta)$ and applying this coordinate map gives

$$\mathcal{R}[\theta] = \theta_\xi + B(\theta)\theta_x + P(\theta) = 0, \quad (19)$$

$$C = \cos\theta - b\sin\theta, \quad B = \frac{\alpha\sin\theta}{C}, \quad (20)$$

$$P = \frac{\alpha\cos\theta\,\phi_x - (\sin\theta + b\cos\theta)\phi_\xi}{W^2 C}. \quad (21)$$

The preliminary velocity gives the initial direction angle θ_0. To obtain the corrected angle $\theta = \theta_0 + \eta$, we solve for the angular correction η with $B_0 = B(\theta_0)$ and $C_0 = C(\theta_0)$ as follows.

$$(\partial_\xi + B_0\partial_x + \beta_0)\eta = -\mathcal{R}[\theta_0], \quad \eta(H) = 0,$$
$$\beta_0 = \frac{\alpha\theta_{0,x}}{C_0^2} + \frac{\alpha b\phi_x - (1 + b^2)\phi_\xi}{W^2 C_0^2}. \quad (22)$$

The predictor uses the corrected direction to update the density and potential through continuity and Poisson at each iteration. For the three-peak wall, doubling the inlet labels from 256 to 512 and the integration steps from 512 to 1024 changes the minimum sampled J from 0.73207 to 0.73235. The maximum ion deflection is 20.46°.

We sample 1201 horizontal sections from $\max h + 0.02L_{sh}$ to $H - 0.02L_{sh}$, with 768 points per section over the full patch. Fourier interpolation in x and cubic interpolation in $\sqrt{\xi}$ give the fields at physical heights. The transverse derivative is taken at fixed z. Doubling the lateral sampling and checking the intervening heights above recovery reproduces the interval maximum to five decimal places in percent.

B. Classification at the inlet

Figure 2 tests the inlet criterion against independent trajectory–Poisson simulations. At the same inlet, predicted and simulated field variations differ by less than 0.001 percentage points across all five walls. Both classify only the three-peak wall (1.48%) below the 5% tolerance.

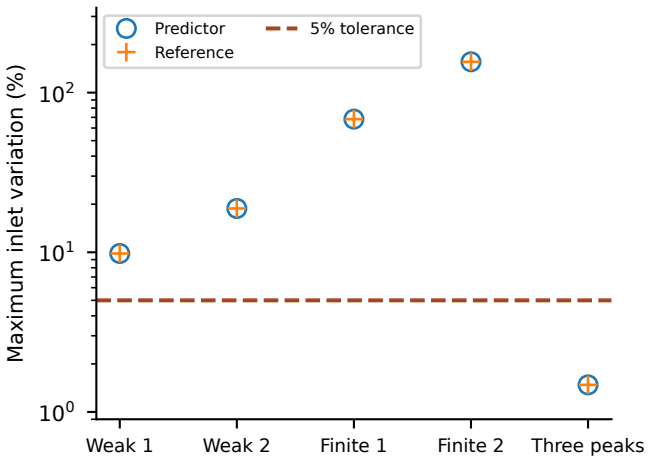


Figure 2. Maximum inlet variation over each full patch, at the same inlet, bias and 5% tolerance. Circles denote prediction and crosses the independent reference. Four fixed-spectrum walls exceed tolerance; the three-peak wall admits the exterior interval in Figure 1.

The largest comparison wall has sheath-scale amplitude $A = \max_{x\in D} |h(x) - \bar{h}| = 0.976 L_{sh}$ and mean peak spacing $2.40 L_{sh}$, yet its inlet variation reaches 155.97%.

TABLE I. Pointwise classification at the common inlet and 5% tolerance. The predictor and the trajectory–Poisson solution give the maximum relative variation of the inlet normal field, $\delta_D(H)$, in percent.

Wall	Prediction	Reference solution	Inlet test
Weak-height 1	9.8272	9.8273	Exceeds
Weak-height 2	18.8140	18.8142	Exceeds
Finite-height 1	68.2257	68.2265	Exceeds
Finite-height 2	155.9693	155.9690	Exceeds
Three unequal peaks	1.4782	1.4782	Passes

C. Effective plane and recovery height for the three-peak wall

Using the three-peak wall in Figure 1 as an example, we demonstrate the validity of Eq. (5) and Eq. (12). The mean inlet field places the effective plane $1.225\lambda_D$ above the mean wall height. With this plane fixed, the predictor and the independent trajectory–Poisson calculation identify the same recovery height on the sampled grid: from $15.661\lambda_D$ toward the inlet, all four fields agree with the planar solution to within 5% at every sampled point. Recovery thus occurs outside the reconstructed sheath edge at $8.119\lambda_D$. The electric field sets the lower limit of agreement. At the sampled height just closer to the wall, its vector error exceeds 5% locally, while the potential and both density deficits remain within tolerance across the patch [Figure 3(b)].

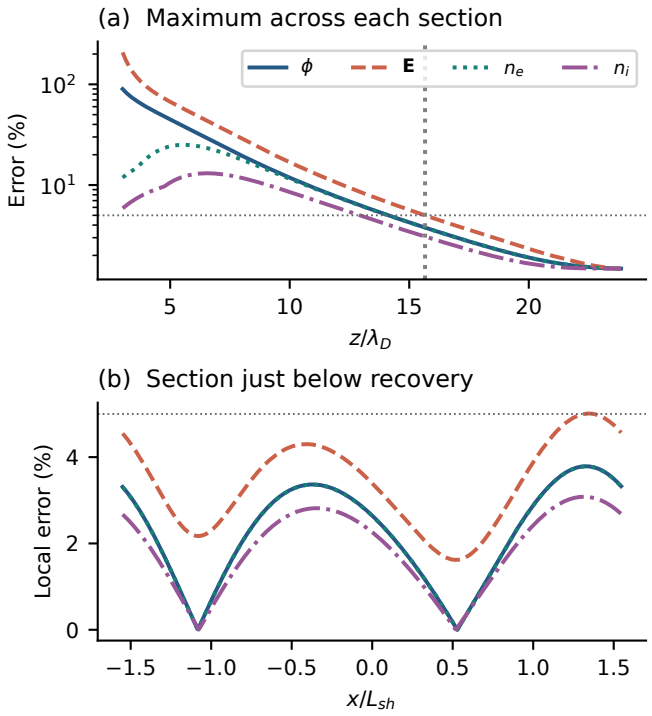


Figure 3. What sets the recovery height on the three-peak wall? (a) Maximum of each normalized error across the patch at each height. (b) Local errors on the section immediately below recovery. The vector-field error crosses 5% near $x/L_{sh} = 1.35$ while both density deficits and the potential already pass.

The predicted mean inlet slope is $\bar{a}_H = 2.2981065 \times 10^{-5}$. Figure 1(c) plots $\max_{k\geq i} e_{\max}(z_k)$, the largest error from height z_i to the last sampled section below the inlet. Both reference grids reproduce the predicted recovery height of $15.661\lambda_D$ (Table II). Figure 3(b) shows what sets the recovery height. One sampled section closer to the wall, at $15.644\lambda_D$, the relative error in the electric-field vector reaches 5.0108% near $x/L_{sh} = 1.35$, exceeding the 5% tolerance.

D. Near-wall transport and particle simulations

The pointwise density formula requires downward flow and a positive horizontal-section Jacobian J. In the four comparison cases, the sampled trajectories cross downward and neighboring trajectories retain their order. Table III gives the smallest sampled J for each wall. We tracked 1536 inlet labels across 96 mapped sections. With x_0 the inlet label and $b = (1 - \xi/H)h'(x)$, the Jacobian at fixed physical height is $J = (\partial x/\partial x_0)|_\xi\,(u_z - bu_x)/u_z$. Using every second label changes each minimum by less than 0.0002.

Figure 4 compares the predicted potential and both species densities with geometry-conforming im-

TABLE II. Three-peak wall. Grid sizes list the number of transverse points followed by the number of mapped vertical points. The sampled recovery height is the lowest sampled height from which all higher sampled sections meet tolerance. The last column gives the maximum error over this interval.

Solution and grid	$\delta_D(H)$ (%)	Recovery height (λ_D)	Maximum error (%)
Predictor 96×121	1.47824	15.66096	4.99568
Reference 96×121	1.47824	15.66096	4.99573
Reference 192×161	1.47824	15.66096	4.99410

TABLE III. Minimum horizontal-section Jacobian on the sampled trajectories for the four comparison walls, using 1536 inlet labels. Here $A = \max|h - \bar{h}|$.

Wall	A/L_{sh}	Minimum J
Weak-height 1	0.061	0.956501
Weak-height 2	0.122	0.919004
Finite-height 1	0.488	0.783207
Finite-height 2	0.976	0.714716

mersed finite element particle-in-cell (GCIFE-PIC) simulations [29].

Figure 4 compares the near-wall potential and both species densities on Finite-height 2 ($A/L_{sh} = 0.976$), the largest comparison wall in Figure 2. The predictions agree well with the reference on this wall. To check the electron response, we evaluate F_e at the particle potential in each of 60 records over $300 < t \leq 360$ (time in λ_D/c_s), project onto the particle-density nodes with the same cloud-in-cell weights, and then average over time. For $0.25\lambda_D \leq z - h(x) \leq L_{sh}$, the volume-weighted relative L^2 error against the time-averaged electron density is 0.690%.

VI. USING THE EFFECTIVE PLANE AND THE TRANSPORT CORRECTION IN FLUID MODELS

The exterior fluid grid starts at z_m, above the sheath edge where all four fields meet tolerance. The classical solution for the effective wall at s_{eff} supplies the interface potential $p = \phi_c(z_m)$. Its first integral relates p and the planar potential slope $g = \phi_c'(z_m) = -E_{z,c}(z_m) > 0$ to the wall-to-interface distance,

$$z_m - s_{\text{eff}} = \int_V^p \frac{d\psi}{\sqrt{g^2 + 2[U(\psi) - U(p)]}}. \tag{23}$$

For the three-peak wall, we start the fluid grid at $z_m = 16\lambda_D$, prescribe p there and zero potential at $H = 24\lambda_D$, and compute the field from the resulting fluid–Poisson solution. Figure 5(a) compares the fluid ion density deficit (curve) with the range across the rough-wall patch (shaded band). Panel (b) compares all four fields point by point with the independent rough-wall reference. The largest sampled error, 4.68% for the electric-field vector, meets the 5% tolerance.

The maximum sampled relative error in the electric-field vector rounds to 4.68% on both the 513- and 1025-node grids.

For near-wall transport on a separate wall of period $8L_{sh}$, the fluid model retains the rough geometry and replaces $f(\phi)$ in Poisson's equation with $n_i = f(\phi)G$. Figure 5(c–e) compares the ion densities from the uncorrected model ($G = 1$), the corrected model, and PIC. Accounting for ion focusing and deflection improves agreement with the PIC density profile. In panel (f), the uncorrected flux per unit projected wall area is uniform. The corrected model captures the variation along the wall observed in PIC.

The particle data in Figures 4 and 5(c–f) were obtained with GCIFE-PIC [29].

VII. CONCLUSIONS

A rough wall yields strongly multidimensional near-wall ion flow, while the exterior plasma may still be described by a single classical sheath. At fixed inlet conditions and tolerance, the inlet-field variation gives the criterion for exterior planar equivalence. The mean inlet field selects the effective wall, and the four-field recovery height sets the extent of pointwise agreement. Where planar equivalence fails, conservation of ion flux along trajectories gives a pointwise correction for the local ion density and wall flux. Independent trajectory–Poisson calculations verify exterior recovery for a sheath-scale wall, and fluid and PIC simulations confirm the predicted variations in near-wall density and wall flux.

ACKNOWLEDGMENTS

This work is supported by the Doctoral Scientific Research Start-up Project of Liaoning Provincial Natural Science Foundation (2026-BS-0078, 2026-BS-0402).

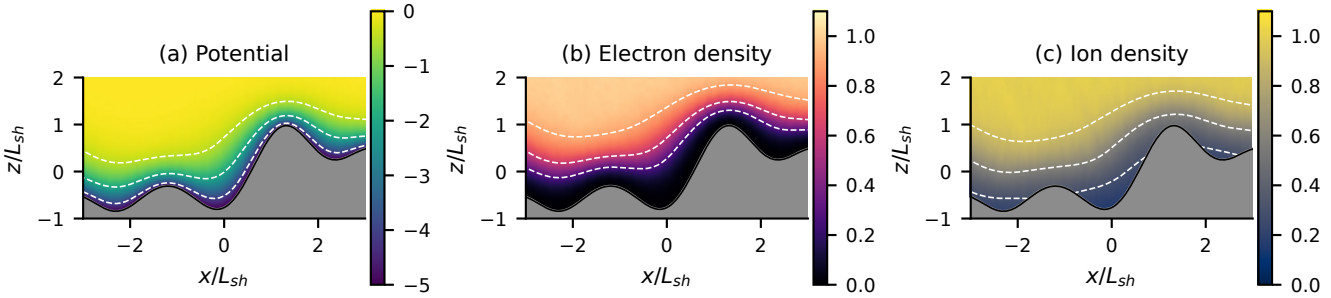


Figure 4. Particle tests of the nonplanar sheath model underlying the boundary reduction. Colors show the electron–ion particle-in-cell results and contours show the independently computed model predictions for (a) potential, (b) electron density, and (c) ion density on equal physical scales. This comparison uses the largest fixed-spectrum wall, whose inlet exceeds tolerance in Figure 2.

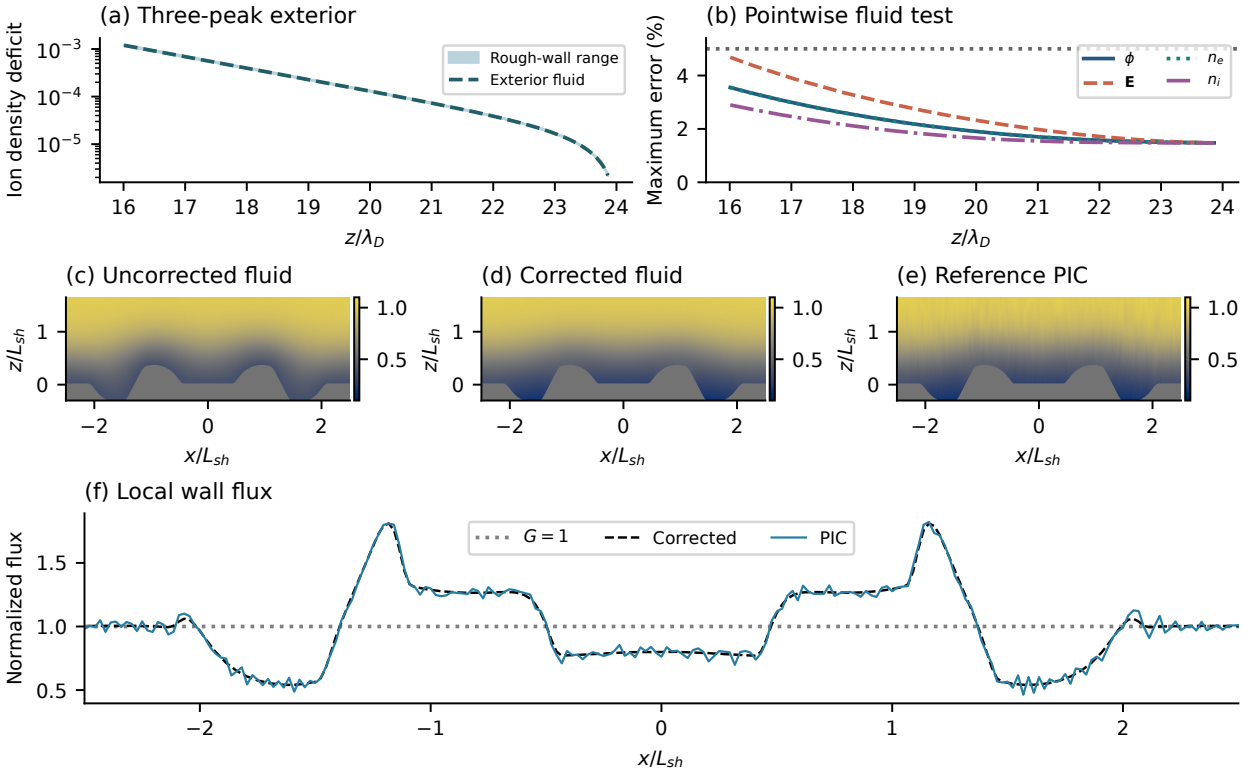


Figure 5. Fluid calculations for the exterior of the three-peak wall (a,b) and for near-wall transport on a separate rough wall (c–f). (a) Exterior fluid ion deficit and the range of $n_0 - n_i$ across the three-peak wall of Figure 1. (b) Maximum fluid error across the patch for each observable at each sampled height. (c–e) Near-wall ion density n_i from the uncorrected fluid model, corrected fluid model, and PIC for a separate wall of period $8L_{sh}$. (f) Local ion flux per unit horizontally projected wall area, normalized by the inlet flux $n_0 M$.

[1] M. A. Lieberman and A. J. Lichtenberg, *Principles of Plasma Discharges and Materials Processing* (Wiley, 2005).

[2] S. D. Baalrud, B. Scheiner, B. T. Yee, M. M. Hopkins, and E. Barnat, Interaction of biased electrodes and plasmas: sheaths, double layers, and fireballs, Plasma Sources Science and Technology **29**, 053001 (2020).

[3] K.-U. Riemann, The Bohm criterion and sheath formation, Journal of Physics D: Applied Physics **24**, 493 (1991).

[4] N. Mellet, Y. Marandet, H. Bufferand, G. Ciraolo, P. Genesio, J. P. Gunn, P. Roubin, E. Serre, and

P. Tamain, Multiscale modelling of sheath physics in edge transport codes, in *26th IAEA Fusion Energy Conference* (2016) paper TH/P6-9.

[5] I. D. Kaganovich, How to patch active plasma and collisionless sheath: A practical guide, Physics of Plasmas **9**, 4788 (2002).

[6] Y. Li, B. Srinivasan, Y. Zhang, and X.-Z. Tang, Bohm Criterion of Plasma Sheaths away from Asymptotic Limits, Physical Review Letters **128**, 085002 (2022).

[7] N. Nuwal, T. Yamauchi, A. Sharma, D. A. Levin, and J. L. Rovey, Kinetic modeling and experiments of a pulsed-bias plasma in a multipole plasma chamber, Physics of Plasmas **29**, 112105 (2022).

[8] J. W. Brooks and R. Dutta, Sheath thickness measurements with the biased plasma impedance probe: Agreement with Child–Langmuir scaling, Physics of Plasmas **33**, 063502 (2026).

[9] X. Wang, H. Lee, S. K. Nam, and M. J. Kushner, Erosion of focus rings in capacitively coupled plasma etching reactors, Journal of Vacuum Science & Technology A: Vacuum, Surfaces, and Films **39**, 063002 (2021).

[10] G. Memos, E. Lidorikis, and G. Kokkoris, Roughness Evolution and Charging in Plasma-Based Surface Engineering of Polymeric Substrates: The Effects of Ion Reflection and Secondary Electron Emission, Micromachines **9**, 415 (2018).

[11] M. Passet, M. Panelli, and F. Battista, Numerical Modeling of Erosion in Hall Effect Thrusters, Particles **7**, 121 (2024).

[12] G. S. Chiu and S. A. Cohen, Comparisons of experimental measurements and two-dimensional plasma-fluid numerical simulations of a magnetized plasma column, Physics of Plasmas **3**, 4250 (1996).

[13] W. Hu, S. Dai, A. Kirschner, and D. Wang, Surface roughness effects on plasma near a divertor plate and local impact angle, Nuclear Materials and Energy **12**, 313 (2017).

[14] V. P. BUDAEV and M. YAKOVLEV, On Fractal Properties of Equipotentials over a Real Rough Surface Faced to Plasma in Fusion Devices, Plasma and Fusion Research **3**, 001 (2008).

[15] D. J. Economou and R. C. Alkire, Effect of Potential Field on Ion Deflection and Shape Evolution of Trenches during PlasmaAssisted Etching, Journal of The Electrochemical Society **135**, 941 (1988).

[16] E. Stamate and H. Sugai, Modal Focusing Effect of Positive and Negative Ions by a Three-Dimensional Plasma-Sheath Lens, Physical Review Letters **94**, 125004 (2005).

[17] E. Stamate and M. Yamaguchi, Fine structure of modal focusing effect in a three dimensional plasma-sheath-lens formed by disk electrodes, Applied Physics Letters **107**, 094106 (2015).

[18] D. Kim, D. J. Economou, J. R. Woodworth, P. A. Miller, R. J. Shul, B. P. Aragon, T. W. Hamilton, and C. G. Willison, Plasma molding over surface topography: simulation and measurement of ion fluxes, energies and angular distributions over trenches in RF high density plasmas, IEEE Transactions on Plasma Science **31**, 691 (2003).

[19] D. Vandembroucq and S. Roux, Conformal mapping on rough boundaries. I. Applications to harmonic problems, Physical Review E **55**, 6171 (1997).

[20] L. I. Daikhin, A. A. Kornyshev, and M. Urbakh, Nonlinear Poisson–Boltzmann theory of a double layer at a rough metal/electrolyte interface: A new look at the capacitance data on solid electrodes, The Journal of Chemical Physics **108**, 1715 (1998).

[21] M. Feldman, S.-Y. Ha, and M. Slemrod, A Geometric Level-Set Formulation of a Plasma-Sheath Interface, Archive for Rational Mechanics and Analysis **178**, 81 (2005).

[22] M. Suzuki and M. Takayama, Stability and Existence of Stationary Solutions to the Euler–Poisson Equations in a Domain with a Curved Boundary, Archive for Rational Mechanics and Analysis **239**, 357 (2021).

[23] I. Schweigert, T. S. Burton, G. B. Thompson, S. Langendorf, M. L. R. Walker, and M. Keidar, Plasma interaction with emmissive surface with Debye-scale grooves, Plasma Sources Science and Technology **27**, 045004 (2018).

[24] J. R. Myra and H. Kohno, Calculation of RF sheath properties from surface wave-fields: a post-processing method, Plasma Physics and Controlled Fusion **61**, 095003 (2019).

[25] P. Chabert and J.-L. Raimbault, Sheath Instabilities Excited by Intense Secondary Electron Emission, Physical Review Letters **135**, 235302 (2025).

[26] A. T. Powis and I. D. Kaganovich, Accuracy of the explicit energy-conserving particle-in-cell method for under-resolved simulations of capacitively coupled plasma discharges, Physics of Plasmas **31**, 023901 (2024).

[27] X.-Z. Tang and Z. Guo, Kinetic model for the collisionless sheath of a collisional plasma, Physics of Plasmas **23**, 083503 (2016).

[28] M. J. Goeckner, J. Goree, and T. E. Sheridan, Measurements of ion velocity and density in the plasma sheath, Physics of Fluids B **4**, 1663 (1992).

[29] P. Qiu and C. Lu, High-order geometry conforming immersed finite element particle-in-cell method for plasma–material simulations with curved interfaces and nonhomogeneous jumps, preprint (2026).